ENVIRONMENTAL RESEARCH
LETTERS

LETTER • OPEN ACCESS

Synthetic aperture radar (SAR) detects large gas seeps in Alaska lakes

To cite this article: Melanie Engram and Katey Walter Anthony 2024 *Environ. Res. Lett.* **19** 044034

ENVIRONMENTAL RESEARCH
LETTERS

LETTER

Synthetic aperture radar (SAR) detects large gas seeps in Alaska lakes

Melanie Engram* and **Katey Walter Anthony**

Water and Environmental Research Center, Institute of Northern Engineering, University of Alaska Fairbanks, Fairbanks, AK, United States of America

* Author to whom any correspondence should be addressed.

E-mail: mjengram@alaska.edu

Keywords: synthetic aperture radar, SAR, lake, methane, ebullition, geologic seep, ^{14}C-depleted methane

Supplementary material for this article is available online

OPEN ACCESS

RECEIVED
21 July 2023

REVISED
17 January 2024

ACCEPTED FOR PUBLICATION
20 February 2024

PUBLISHED
20 March 2024

Abstract

Reservoirs of ^{14}C-depleted methane (CH_4), a potent greenhouse gas, residing beneath permafrost are vulnerable to escape where permafrost thaw creates open-talik conduits. However, little is known about the magnitude and variability of this methane source or its response to climate change. Remote-sensing detection of large gas seeps would be useful for establishing a baseline understanding of sub-permafrost methane seepage, as well as for monitoring these seeps over time. Here we explored synthetic aperture radar's (SAR) response to large sub-permafrost gas seeps in an interior Alaskan lake. In SAR scenes from 1992 to 2011, we observed high perennial SAR L-band backscatter (σ^0) from a ~90 m-wide feature in the winter ice of interior Alaska's North Blair Lake (NBL). Spring and fall optical imagery showed holes in the ice at the same location as the SAR anomaly. Through field work we (1) confirmed gas bubbling at this location from a large pockmark in the lakebed, (2) measured flux at the location of densest bubbles (1713 ± 290 mg CH_4 m^{-2} d^{-1}), and (3) determined the bubbles' methane mixing ratio (6.6%), radiocarbon age (18 470 ± 50 years BP), and $\delta^{13}C_{CH4}$ values (−44.5 ± 0.1‰), which together may represent a mixture of sources and processes. We performed a first order comparison of SAR σ^0 from the NBL seep and other known sub-permafrost methane seeps with diverse ice/water interface shapes in order to evaluate the variability of SAR signals from a variety of seep types. Results from single-polarized intensity and polarimetric L-band SAR decompositions as well as dual-polarized C-band SAR are presented with the aim to find the optimal SAR imaging parameters to detect large methane seeps in frozen lakes. Our study indicates the potential for SAR remote sensing to be used to detect and monitor large, sub-permafrost gas seeps in Arctic and sub-Arctic lakes.

1. Introduction

Arctic permafrost imperfectly traps reservoirs of ^{14}C-depleted methane (Isaksen *et al* 2011), a powerful greenhouse gas with a global warming potential of 25–34 times higher than carbon dioxide (Myhre *et al* 2013). This entrapment of methane by permafrost and glacial overburden has been referred to as the 'cryosphere cap' (Walter Anthony *et al* 2012, Kohnert *et al* 2017, Kleber *et al* 2023). However, fractionated hydrocarbons in surface soils near Prudhoe Bay, Alaska is evidence of gas migration through thick, frozen soils, indicating that ice-bonded permafrost is not a perfect seal (Masterson *et al* 2001). Warming and thinning of permafrost, often accelerated by surface and ground water dynamics (Yoshikawa and Hinzman 2003, Woo 2012), can create thawed chimneys in the frozen ground (open taliks) facilitating gas migration (Bowen *et al* 2008, Sullivan *et al* 2021). ^{14}C-depleted methane also escapes to the atmosphere through faults (Etiope and Klusman 2002), and petroleum exploration/extraction often punctures within- and sub-permafrost methane reservoirs causing blowouts (Yakushev and Chuvilin 2000) indicating high volume sub-permafrost gas reservoirs. Anomalously-high methane fluxes observed in a terrestrial sedge-dominated tundra environment (>1100 mg CH_4-C m^{-2} d^{-1}) were attributed to a

thermogenic, sub-permafrost origin (von Fischer *et al* 2010). Whether or not natural ^{14}C-depleted methane emissions are increasing is a matter of great uncertainty (Etiope and Klusman 2002, Schwietzke *et al* 2016), as well as of twofold interest: ^{14}C-depleted methane seeps cause a positive feedback to climate warming by enhancing more warming, thaw, and methane release (Walter Anthony *et al* 2012, Kohnert *et al* 2017); additionally, a solid knowledge of natural ^{14}C-depleted methane emissions is vital to an accurate estimate of anthropogenic methane emissions from petroleum industries (Mazzini *et al* 2021).

Visibly-open holes in lake ice from naturally-occurring bubbling seeps have been used to map and quantify ^{14}C-depleted methane within Alaskan and Greenland lakes (Walter Anthony *et al* 2012, 2021, Sullivan *et al* 2021). Ice holes are created by a combination of vigorous bubbling's mechanical force and water-column convection, whereby relatively warmer lake-bottom water accompanies gas bubbles as they rise to the surface. However, consistent detection, quantification, and monitoring of these high-flux, focused gas seeps on frozen lakes using optical remote sensing approaches is challenging because even a thin layer of ice or snow renders seeps optically undetectable in aerial flights and multispectral satellite imagery. Seeps are also challenging to visually detect in summer during ice-free conditions when rain or breeze on open water obscures bubble-stream visibility.

Recent advances in aerial reconnaissance using multispectral absorption instruments such as the next generation airborne visible/infrared imaging spectrometer (AVIRIS-NG) have successfully mapped geologic methane seeps in the four corners region of the United States (Frankenberg *et al* 2016) and thousands of other terrestrial methane anomalies in the permafrost regions of Alaska and NW Canada (Elder *et al* 2020, 2021). While airborne methane sensors have made important recent advances by mapping over 70 000 km^2 of Alaska and northwestern Canada with AVIRIS-NG during the summers of 2017–2019 through NASA's arctic boreal vulnerability experiment (ABoVE) (Miller *et al* 2019), they remain a terrestrial (not aquatic) methane monitoring platform due to radiometric constraints on spectrometry and are generally relegated to summer flights. Airborne eddy covariance platforms (Kohnert *et al* 2017) can detect both terrestrial and aquatic methane, and have inferred natural-gas methane during summer campaigns based on high, focused fluxes; however, such campaigns have so far been rare and ground-truth limited due to logistical constraints. If methane previously impeded by permafrost can escape through newly formed conduits, greenhouse gas concentration in the atmosphere would increase in a way that is not currently accounted for in carbon budgets. Hence there is a need for development of satellite remote-sensing methods coupled to ground-truth sampling that can accurately detect and quantify large methane seeps to establish a baseline for change detection in vast Arctic landscapes.

Mapping gas seeps with remote sensing could also benefit the safety of people traveling in winter since bubbling creates dangerous ice conditions. The bubbling-induced weak ice is often masked by snow, giving no indication to travelers until they have fallen through the ice.

Synthetic aperture radar (SAR) remote sensing has been used for decades to gain knowledge about lakes and lake ice (Murfitt and Duguay 2021), including an empirical model used to quantify methane bubbling from ecologic sources (microbial methane formed in near-surface sediments) based on the bubble-induced rough ice/water interface in lakes (Engram *et al* 2020), to which SAR is sensitive (Atwood *et al* 2015). While SAR can be more difficult to interpret than multispectral/optical imagery, its active microwave instrument is not dependent on reflected sunlight. Thus, SAR can image lake ice throughout the dark winter, and can penetrate clouds and dry snow. Based on our observations of high sigma-naught (σ^0) normalized radar cross section backscatter features from lake ice at the location of known geologic seeps (Walter Anthony *et al* 2012, Wooller *et al* 2012, Sullivan *et al* 2021) in L-band SAR ($\sim$24 cm wavelength), we were motivated to explore the potential and lay the groundwork for space-borne SAR to systematically detect large gas seeps within lakes. We focus our work on NBL, an interior Alaska lake in which we observed perennial high SAR L-band σ^0 backscatter from a $\sim$90 m-wide anomalous feature in winter ice prior to any field-work knowledge (figures 1(a) and (b)).

The primary goal of this research was to improve our ability to detect and quantify anomalously large gas seeps in frozen lakes by using SAR to gain better understanding of the sensitivity to seepage of a variety of SAR platforms. Specific objectives included: (1) conduct field work to confirm that the remotely-sensed feature at NBL was a large, geologic gas seep; (2) determine optimal parameters for NBL seep detection using single-polarization (single-pol) L-band SAR backscatter with different incidence angles; (3) examine decomposed quadrature-polarized (quad-pol) L-band data from the NBL seep as well as from other known sub-permafrost methane seeps with different ice/gas morphologies (figure 2) in two other Alaskan lakes to gain first-order knowledge of how different shapes of ice/water interfaces present in SAR polarimetric parameters; (4) examine shorter wavelength C-band SAR over the NBL seep to determine whether large methane seeps could be detected with this wavelength, since low C-band backscatter (instead of high) anomalies had suspected (no ground truth) association with

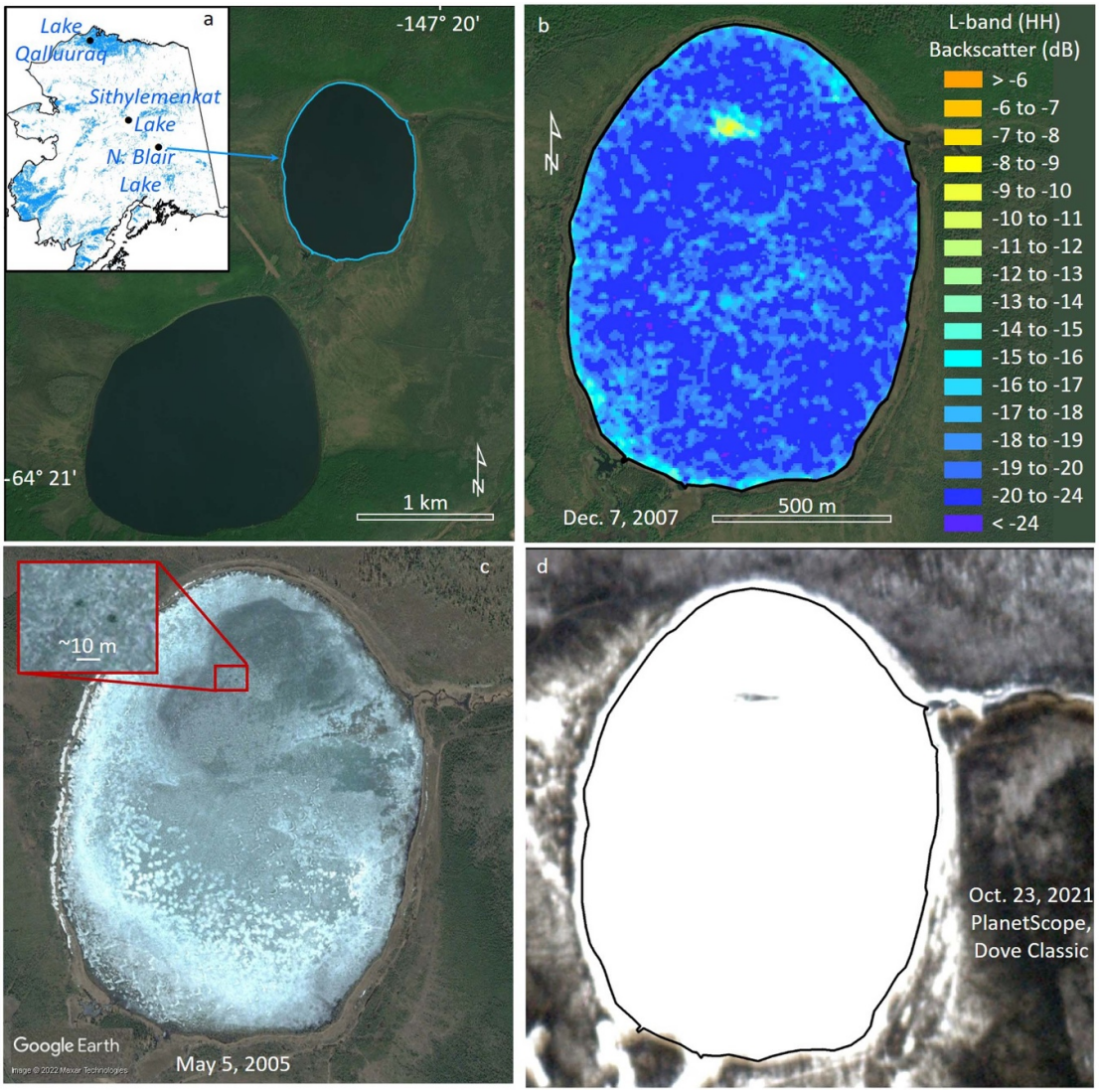

Figure 1. North Blair Lake (NBL) in interior Alaska is the site of a large methane seep discovered exclusively with L-band SAR imagery. The NBL area is used for recreation and hunting, although the land is in an Army reservation, labelled 'Fort Wainwright' on a USGS map (US Geological Survey, Fairbanks B-1, 1:63 360). Lake Qalluuraq and Sithylemenkat Lake are sites of known large methane seeps (panel (a)). High L-band HH-polarization backscatter feature in northern quadrant of NBL (panel (b)) corresponds to open holes in the ice in fall (panel (c)) and spring (panel (d)) optical imagery (Image © 2021 Planet Labs PBC). Lakes (blue) shown in panel (a) are HydroLAKES dataset (Messager *et al* 2016). SAR data in panel (b) is ALOS PALSAR-1 ©JAXA/METI 2007, colorized for contrast and normalization between images. Background image in panels (a) and (b) from Alaska High Resolution Imagery RGB 2020 (Maxar Technologies Inc., Alaska Geospatial Office, USGS). (a) Data reproduced from Alaska Department of Natural Resources.
 Data reproduced from Messager *et al* (2016). (b) Data reproduced from ALOS PALSAR-1 ©JAXA/METI 2007. Background image: ©2020 Maxar Technologies Inc., Alaska Geospatial Office, USGS.

natural gas seepage in a West Siberian lake (Pointner *et al* 2021); and (5) examine historical L-band data to determine the NBL seep presence or absence in the early 1900s (supplementary tables 1 and 2).

We used only ice-on SAR scenes for analysis, since σ^0 from bubbling activity in open water can be obscured by wind-roughened water surfaces. In addition to the physical presentation of these seeps as they effect the highly reflective ice/water interface, we present results of gas analyses from the seeps.

2. Methods

2.1. Physical properties of study site and comparison of lake seeps

NBL is one of two 'Blair Lakes' that are morphologically unusual (exceptionally large and round) on the Tanana River floodplain landscape, an area noted by Jorgenson *et al* (2001) as Tanana-Blair Lakes Uplands (figure 1(a)). Blair Lakes are partially surrounded by hills >300 m high with steep terrain (supplementary figure 1). Hills in this region can

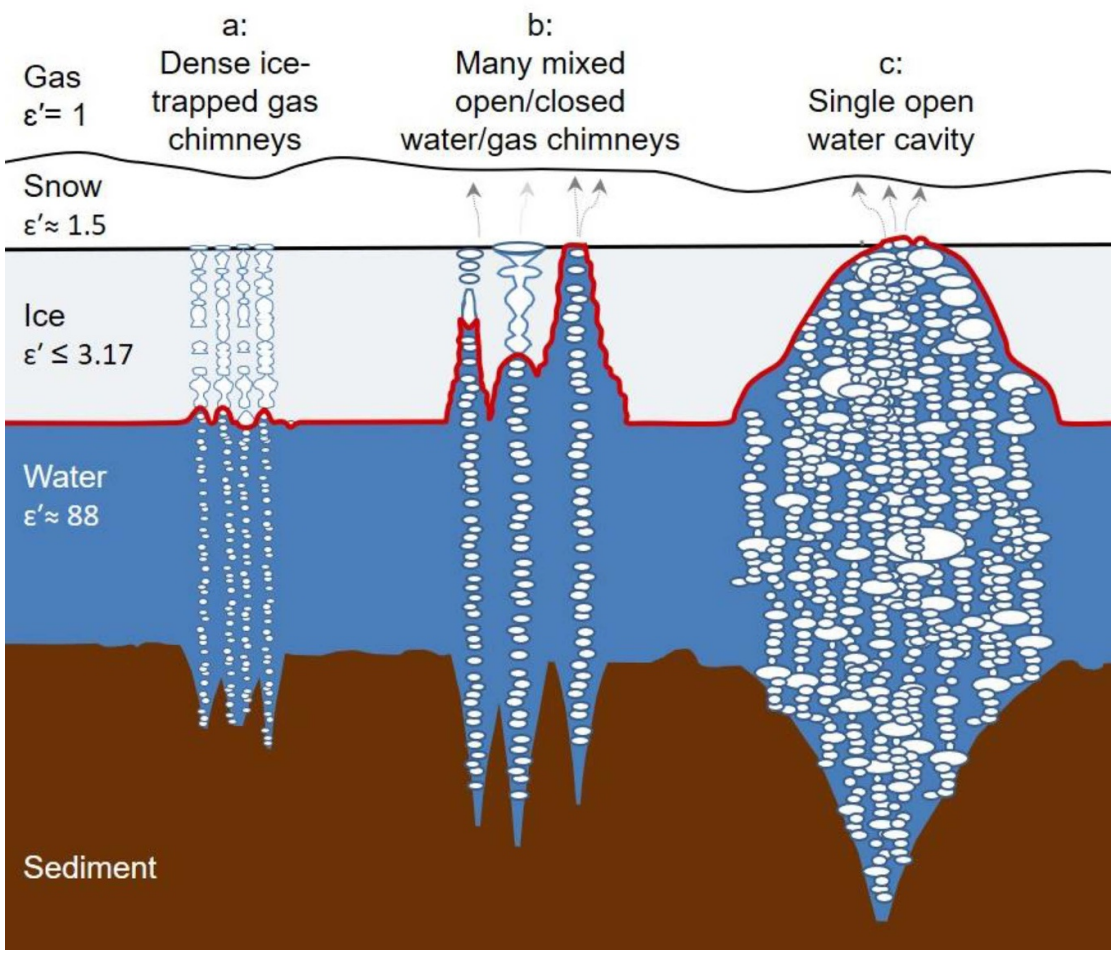

Figure 2. Schematic showing probable shapes of gas, water, and ice for studied seeps. Red line shows highest dielectric contrast between two media, indicating probable location of SAR scattering. The NBL seep represents (a) closed ice surface with bubbles included in dense ice-trapped chimneys (sometimes open holes in shoulder seasons). The north seep at Lake Qalluuraq (b) has many mixed open/closed water/gas chimneys. The main seep at Lake Qalluuraq (c) is a single open water cavity. Shapes of bubbles in ice for (a) and (b) are modeled after bubbles observed in ice blocks harvested from lakes near Fairbanks with bubble size of <5 mm and 1–2 cm respectively. Shape of ice cavity in (c) is based on under-ice photos in Walter *et al* (2009). Ice growth changes the shape of the ice/water/gas interface over time. Pockmarks in sediments are not to scale, but indicate relative differences based on field observations.

create large precipitation gradients with permafrost-free highlands serving as groundwater recharge zones to the permafrost-dominated lowlands where Blair Lakes reside (Kane 1981, Gieck and Kane 1986, Youcha 2003).

The origin of Blair Lakes is unknown. They are not of glacial or thermokarst origin (Kurtz *et al* 1966) and there are no volcanos nearby to indicate they are maars, a specific round type of waterbody caused by the explosive reaction of hot lava with water or permafrost (Lorenz 1973, Beget *et al* 1996). NBL overlays non-Yedoma soils (Strauss *et al* 2022): permafrost in the Blair Lakes study area (47 m thick in one borehole, Chacho *et al* 1995) is discontinuous (Jorgenson *et al* 2008) and undergoing rapid degradation (Jorgenson *et al* 2001).

Faults form fractures through which geologic methane can vent (Etiope and Martinelli 2002), and the occurrence frequency of lake-bound geologic methane seeps inversely correlates with distance to faults (Walter Anthony *et al* 2012). Blair Lakes are in the Salcha seismic zone, and a fault mapped approximately 4.3 km N-NE of the NBL seep (Gedney and VanWormer 1974, supplementary figure 1) is a left-lateral slip fault that could contribute to gas release in NBL (Barrett Salisbury, personal communication).

In addition to the NBL seep, we selected previously identified geologic seeps with different ice-bubble morphologies (figure 2) to explore variability in geologic seep interactions with SAR. We chose examples of three types of geologic seep morphologies in lake ice that we have previously measured *in situ* (figure 2) and examined scattering mechanisms from decomposed quad-pol SAR data. Lakes where these seeps occur were not necessarily representative of particular lake types, but were chosen because they contained large, sub-permafrost methane seeps that created a variety of shapes at the ice/water interface

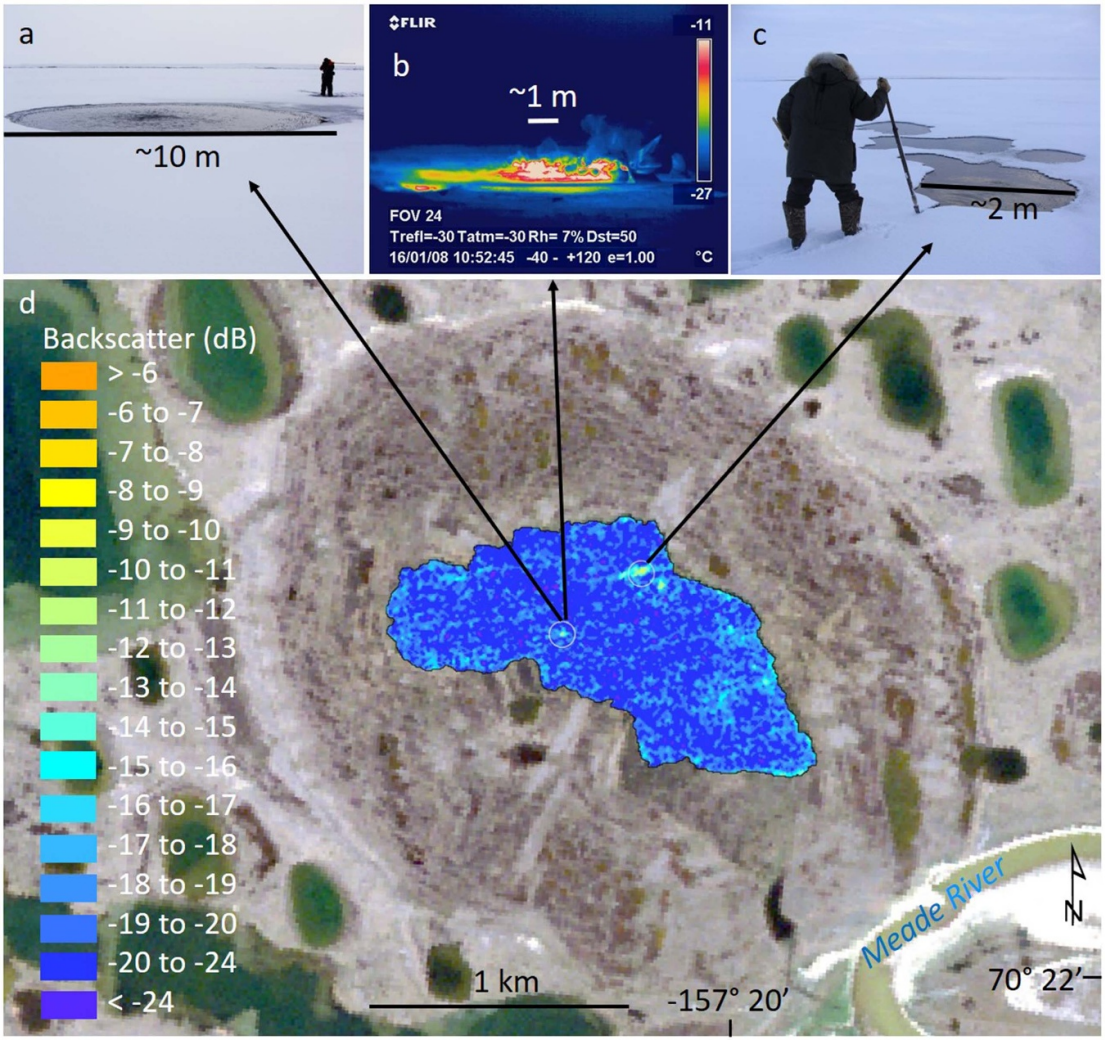

Figure 3. Qalluuraq L. main gas seep (a) 8 October 2008 open hole in lake ice caused by vigorous bubbling. For scale, the person is slightly over six feet tall. Photo reused with permission from co-author Katey Walter Anthony. (b) Forward looking InfraRed (FLIR) image of researcher measuring gas flow rate on 18 January 2008 from a small hole made in the naturally-occurring snow-ice cover. The warm pixels indicate thin, <10 cm snow-ice cap over the ice-free hole created by gas seepage. Photo reused with permission from Peter Anthony. (c) Lake Q North seep, 8 October 2008. Panels (a)–(c) are modified from Walter *et al* (2009). Photo reused with permission from co-author Katey Walter Anthony. (d) PALSAR-1 SAR image acquired 30 January 2010 (Data reproduced from ALOS PALSAR-1 ©JAXA/METI 2010.) showing high backscatter from Q Main and Q North seeps. A drained lake basin surrounding the lake is visible in the background image 7 July 2007, true color (Data reproduced with permission from ©JAXA 2007. All rights reserved.).

which could affect SAR backscatter. Seep-type, rather than lake-type, is considered representative in the Arctic.

Two seeps occurred in Qalluuraq Lake, a thermokarst lake situated in a larger drained lake basin near the Meade River south of Atqasuk, Alaska: (1) a large (~10 m diameter) seep, called *Q. Main* (figures 3(a) and (b)) that creates a single cavity in the ice, remaining ice-free (open) with vigorous bubbling in winter despite sub-zero temperatures although a thin (<10 cm in January 2008) snow-ice cover seasonally masks the open hole at the surface (Wooller *et al* 2012), (2) a seep field in the north section of the lake (*Q. North*) that creates numerous mixed open/closed water/gas chimneys (figure 3(c)) in the lake ice on the order of 1–2 m in diameter (Walter Anthony *et al* 2012).

Additionally, we selected two methane seeps at Sithylemenkat Lake (figure 4), which manifest as open holes in lake ice throughout winter, surrounded by a belt of ice-trapped bubble columns, thereby representing all three types of water-ice-bubble shapes shown in figure 2. Sithylemenkat Lake has a round shape similar to NBL and is also mostly surrounded by hills. Walter Anthony *et al* (2012) conducted field work at this lake on 16 February 2010 when the ice was >2 m thick: the gas had a strong hydrogen-sulfide (rotten egg) smell. Water depth at the southern

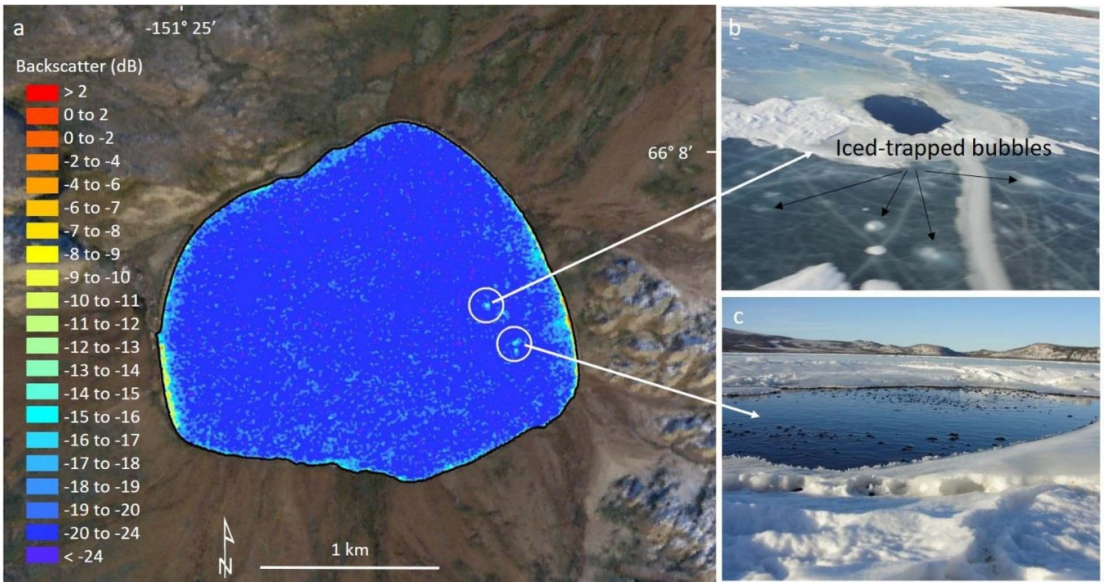

Figure 4. (a) SAR L-band mid-winter single-pol image (15 February 2009; Data reproduced from ALOS PALSAR-1 ©JAXA/METI 2009.) of frozen Sithylemenkat Lake shows high backscatter at the location of open holes as measured on-ice by GPS (white circles) on 16 February 2010. (b) Larger of the two open holes as seen from the air with ice-trapped bubbles in the >2 m thick adjacent ice. (c) Smaller of two naturally-occurring open holes caused by ebullition. Areas of the small (c) and large (b) holes were estimated in the field to be 6 m^2 and 21 m^2 respectively. All rights reserved. Photo reused with permission from co-author Katey Walter Anthony. Background image for (a) is AVNIR-2 27 September 2010 true color. Data reproduced with permission from ©JAXA 2010. All rights reserved.

Table 1. North Blair Lake seep bubble gas concentrations and isotopes (this study) alongside those constituents previously measured at Qalluuraq Lake (Lake Q, Walter Anthony *et al* 2012) and Sithylemenkat Lake (this study).

		North Blair Lake				
Bubble constituent		Ice-trapped bubbles 18 December 2020	Fresh bubbles 11 September 2021	Sithylemenkat Lake Fresh bubbles 16 February 2010	Lake Q (main seep) Fresh bubbles 2007–2009	Lake Q (north seep) Fresh bubbles Oct. 9 October 2008
CH_4	(%)	5.4	6.6	5.5 ± 0.0	97.0 ± 3.6	99.5 ± 1.2
CO_2	(%)	0.5	0.3	0.09 ± 0.00	1.17 ± 0.23	0.38 ± 0.10
Ethane	(%)	—	—	0.0099 ± 0.0010	0.0517 ± 0.0474	0.0021 ± 0.0001
$\delta^{13}C_{CH4}$	(‰)	−48.1 ± 0.02	−44.5 ± 0.1	−48.4 ± 0.76425	−57.22 ± 1.20	−57.40 ± 0.29
δD_{CH4}	(‰)	−212.2 ± 0.44		−214.3 ± 0.9385	−231.22 ± 1.35	−226.38 ± 2.69
$^{14}C_{CH4}$ age	(yrs BP)		18 470 ± 50	38 300 ± 400	47 380 ± 4,580	47 511 ± 1,400
	(FM)		0.1003 ± 0.0006	0.0085 ± 0.0004	0.0027 ± 0.0016	0.0027 ± 0.0005
$^{14}C_{CO2}$ age	(yrs BP)		6,370 ± 80	—	—	—
	(FM)		0.4525 ± 0.0040	—	—	—
CH_4 flux	kg CH_4 d^{-1}		0.18	1.2	98	8.0

seep was 12.9 m. The origin of Sithylemenkat Lake is undetermined: some claim it is a crater lake formed when a meteor struck Earth (Cannon 1977, 1978) while others dispute this theory (Patton and Miller 1978). Gas geochemistry is shown in table 1.

2.2. Field work on NBL

Garmin-GPS coordinates for field samples and observations were collected on NBL during three field campaigns on 18 December 2020; 10–11 and 17 September 2021. During the 10–11 September 2021 field work, bubbling extent was mapped from a boat during calm water conditions when seep-bubble streams were visible in the lake water column (figures 5(a) and (c)). Seep-field area was calculated in GIS (ArcMap v.10.7) and active-bubbling waypoints were overlain with SAR data in GIS to compare the location and extent of the mapped seep field to the high-backscatter feature (figure 6(b)).

Concentrations of methane and carbon dioxide in December ice-trapped and September open-water bubble samples were measured by gas chromatography at Florida State University (supplementary methods). We mapped NBL bathymetry 10–11 September 2021 using a boat-mounted side-scan sonar unit with integrated GPS (supplementary methods). During September 2021 fieldwork, methane and carbon dioxide linear fluxes were measured

Figure 5. September 2021 field observations at N. Blair L. included flux measurements with a floating chamber attached to a LGR-ICOS microportable greenhouse gas analyzer (a), bathymetric measurements, and collection of gas samples with underwater bubble traps (b). Active bubbling is seen on lake surface (b), (c) and was mapped at the location of the high L-band SAR backscatter anomaly. No evidence of oil or oil slicks were seen at NBL. (a) Photo reused with permission from Peter Anthony. (b), (c) Photo reused with permission from co-author Katey Walter Anthony.

continuously for ∼2-to ∼4 min at 14 locations within the active bubbling area and around the lake outside the seep field using the floating static chamber method (Aguirrezabala-Campano *et al* 2021; figures 5(a), 6(a) and supplementary table 3).

To explore possible differences in water chemistry at the seep and remainder of the lake we measured water-column hydrochemical properties with a Quanta Hydrolab (supplementary table 4) and surface-water δD_{H2O} and $\delta^{18}O_{H2O}$ on 11 and 17 September 2021 (figure 6(a)) at the Alaska stable isotope facility (supplementary table 5).

2.3. SAR data processing and analysis

To assess the seasonal variation and historic duration in σ^0 presentation of the NBL seep, we processed data from two L-band spaceborne SAR missions over NBL: the Phase Array L-band Synthetic Aperture Radar-1 (PALSAR-1) instrument aboard the Japanese Advanced Land Observing Satellite-1 (ALOS-1) from 2006–2011, and the Japanese Earth Resources Satellite 1 (JERS-1) from 1992–1998 (supplementary methods). The range of σ^0 for JERS-1 and PALSAR-1 single-pol (HH) imagery was determined by the minimum and maximum pixel values within the seep area, mapped from field work, for different incidence angles and seasons (early-, mid-winter, and Spring) (tables 2 and 3). As well as σ^0 intensity, we visually examined σ^0 contrast between the seep and adjacent ice in images acquired with different incidence angles to determine optimal imaging parameters for detecting seeps.

To compare NBL with previous published research reporting low C-band SAR backscatter from suspected West Siberian lake seeps, we processed and examined Sentinel-1 C-band (∼5 cm wavelength) dual polarized (dual-pol) data over NBL for the 2020–2021 winter, coinciding with 18 December 2020 field work (SI methods). The approximate area of the perennial high-backscatter feature in NBL was calculated in GIS from several scenes throughout the winter by manually delineating the high-backscatter feature from the low-backscatter background, then calculating the area.

We processed all quad-pol PALSAR-1 scenes when NBL was frozen, using the [**T3**] coherence matrix main diagonal elements and the Yamaguchi 3-component decomposition (Yamaguchi *et al* 2006) in order to include a mathematical as well as an incoherent model-based decomposition in our analysis (Ferguson and Gunn 2022). The resulting three Yamaguchi components (odd-, double-bounce and volumetric scattering) along with the $T11$, $T22$, and $T33$ parameters were processed to geotiff files (SI methods). To compare the NBL seep to known seeps in Lake Qalluuraq and Sithylemenkat Lake, which have different ice/water interface shapes, we downloaded and decomposed all quad-pol data for these

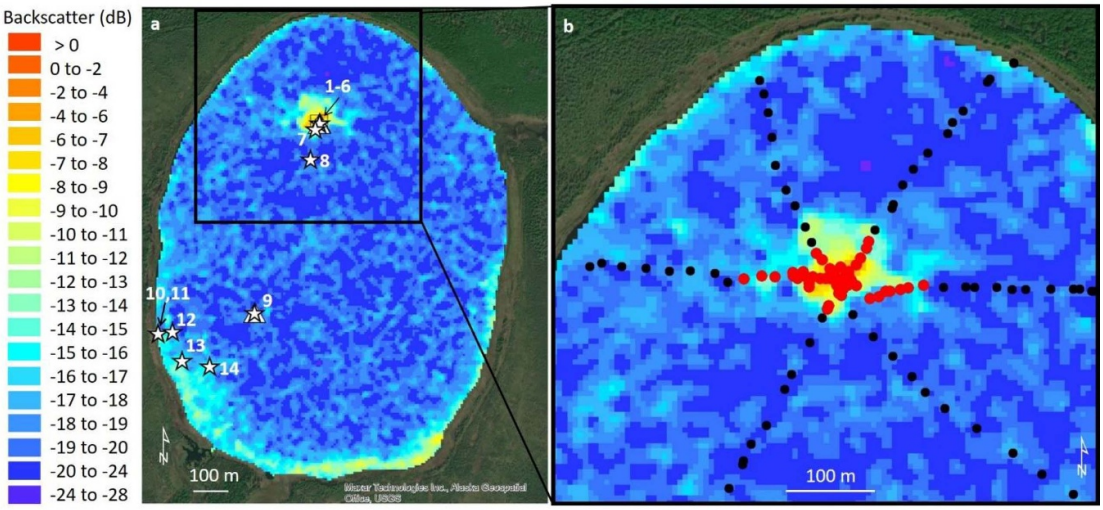

Figure 6. PALSAR-1 single-pol image on 17 March 2011 of NBL (a) showing chamber flux measurement locations as white stars (numbers correspond to supplementary table 3), bubble trap location as small square inside seep (at points 1–6), hydrolab locations as white triangles (at points 9 and 1–6). (b) GPS points recorded from a boat in September 2021 at locations of bubbling (red circles) and locations of no bubbling (black circles) align spatially with location of 2006–2011 SAR high backscatter zone. Data reproduced from ALOS PALSAR-1 ©JAXA/METI 2011. Background image: ©2020 Maxar Technologies Inc., Alaska Geospatial Office, USGS.

lakes using the same processing methods as for NBL. Using a generalized seep shape derived from multiple images, we calculated the mean backscatter from the seep and the adjacent surrounding ice (100 m), and additionally performed a first order visual assessment of the presence/absence of each polarimetric component from these seeps with different ice-water interface shapes (table 4).

3. Results and discussion

3.1. Field work

3.1.1. Bathymetry and seep areal extent

Field work confirmed continuous streams of bubbles at the SAR-detected NBL anomaly (figure 5). The areal extent of the seep field from field observations was 8057 m^2 (∼90 m in diameter). Lake depth was ∼1–4 m across most of NBL (mean depth 2.2 m), except directly below the seep field, where a complex pockmark up to 8 m deep was mapped (figures 7(a) and (b)). In published literature, at least two similar pockmarks are reported below large gas seeps releasing sub-permafrost, geologic methane through narrow thaw conduits beneath lakes: Bowen *et al* (2008) reports a pockmark up to 9.5 m in depth (∼35 m diameter) on the Mackenzie River Delta; Sullivan *et al* (2021) describes a 15 m deep pockmark (∼32 m diameter) in northwest Alaska. At NBL, side-looking sonar imaged bubbles rising from pockmarks (figure 7(c)). Some pockmarks have been attributed to groundwater springs associated with permafrost thaw (Paull Charles *et al* 2022). Sullivan *et al* (2021) gives a comprehensive review of pockmarks associated with methane release in the marine, terrestrial, and freshwater realms.

3.1.2. Estimating seep emissions using floating chambers

In most lakes, ebullitive events impede measurement of linear concentration increases in chambers; however, due to the steady stream of small (<0.5 mm) bubbles in the NBL seep, we obtained linear fluxes (R^2 = 0.93–0.99); although the linearity of diffusive fluxes outside the seep field was higher: R^2 = 0.98–0.99 (supplementary table 3, supplementary figure 2). Under calm open-water conditions, field workers estimated that the density of ebullition bubbles at the location where the floating chamber measurements were made was about 100 times higher than the rest of the seep field, as defined by bubbling extent observed by GPS mapping (figure 6(b)).

Two areas (approx. 3 m × 4 m each) within the seep field had particularly strong ebullition. Ebullition within the densest bubbling area was ∼1700 mg CH_4 m^{-2} d^{-1}. When chambers were placed over open water areas between bubbling streams in the seep field, the diffusive flux was much lower, 14 ± 6 mg CH_4 m^{-2} d^{-1}, indicating ebullition dominated total emissions from the seep field. This also indicates that in the most intense areas of bubbling, seep emissions are 41 times higher than diffusion measured by floating chambers outside the seep field on the rest of the lake (42 ± 36 mg CH_4 m^{-2} d^{-1}). Ecological methane ebullition in NBL

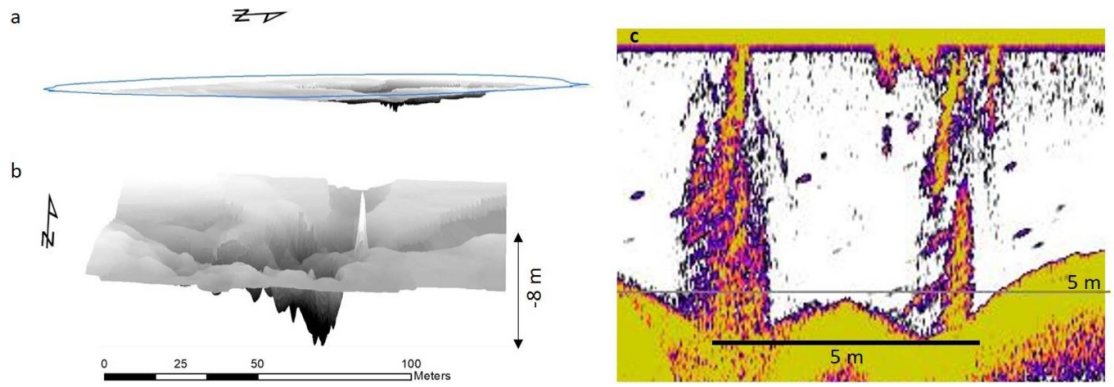

Figure 7. Whole-lake bathymetry (a) shows complex pock-mark (b) directly beneath the seep. Note vertical scale is ten times horizontal scale (a), (b). Sonar image (c) acquired 17 September 2021 showing bubble plumes rising from pockmarks in one of the densest seep areas of NBL.

associated with microbial decomposition of organic matter in surface lake sediments was not measured, but sporadic bubbling of larger diameter bubbles (<2 cm) were observed in various areas of NBL away from the seep field during September field work.

3.1.3. Gas analysis results

Methane content of the NBL seep bubbles was unusually low (6.6%) compared to geologic seeps associated with coalbed and petroleum hydrocarbons (typically 40%–100%); however, the magnitude of seepage on a volumetric basis (figure 8(a)), as well as the ^{14}C-depleted CH_4 [18 470 ± 50 years BP; 0.1003 ± 0.0006 Fraction Modern (FM)] (figure 8(b)) and $\delta^{13}C_{CH4}$ values (−44.5 ± 0.1‰) (figure 8(c)) indicate that it is more similar to other geologic methane seeps in Alaska than to ecological sources. Carbon dioxide concentration (0.3%) was even lower than methane, but carbon dioxide concentrations are often well below 1% in Alaska lake bubbles (Walter Anthony *et al* 2012, 2021). Interestingly, the methane concentration and stable isotopes at NBL were most similar to bubbles emitted from Sithylemenkat Lake (table 1), also a strikingly round lake, located in the Brooks Range.

The NBL seep-field bubbles were <5 mm in diameter at the water surface, smaller than bubbles typically seen at other geologic methane seeps (1 to >5 cm diameter bubbles and plumes of coalesced bubbles ∼100 cm diameter, Walter Anthony *et al* 2012). Geologic methane seeps are characterized by one or more continuous streams of bubbles (as seen at the NBL seep), in contrast to temporally sporadic ebullition from ecologic sources of methane, which intermittently release bubbles. Geologic methane seeps are also characterized by high fluxes of up to 141 600 l gas seep^{-1} d^{-1} often with high concentrations (up to 99.5%) of highly ^{14}C-depleted methane (Walter Anthony *et al* 2012, Sullivan *et al* 2021).

3.2. SAR results and discussion

3.2.1. SAR backscatter from ice over liquid water

L-band SAR backscatter depends mainly on the physical shape of the ice/water interface created by gas bubbling, since cold water has a high dielectric constant ($\varepsilon' = \sim 88$, Komarov *et al* 2005) compared to pure ice ($\varepsilon' = \sim 3.17$, Mätzler and Wegmüller 1987). This large dielectric contrast causes a highly reflective ice/water interface (figure 2). Field observations reveal that gas seeps in northern lakes sculpt the ice/water interface in several different ways. Strong, focused seeps with continuous bubble streams cause convection of the water column, whereby warm lake-bottom water is entrained by rising bubbles, impeding surface lake-ice formation. Since the water column surrounding strong bubble streams is not affected by ebullitive turbulence, lake ice grows vertically downward in calm water surrounding seeps. The result is a chimney of bubbling water with irregularly shaped ice walls (figure 2). Whether there is one focused seep or many seeps in a seep field will determine the number, diameter, and density of venting water-filled columns in lake ice, which in turn affect roughness relative to the SAR wavelength.

Ebullition rate, in combination with air temperature and snowfall, determine whether ice forms at the lake surface (Zimov *et al* 2001). Often, bubbling rates are not strong enough to keep the ice totally 'open' all winter: often a thin, incomplete layer of ice forms over the open bubbling water, while sometimes the surface completely freezes over. In cases where seeps ice-over, emerging bubbles displace the water and the mostly ice-free chimneys fill, or partially fill, with gas that periodically escapes though small crack and fissures in the ice surface, and then refill with gas by continued bubbling. Some seeps are highly diffuse (e.g. NBL), with widely-distributed bubble streams creating bubble-chimneys that become mostly encapsulated in the lake-ice sheet. The insulating effect of ice-trapped gas causes an upward-warped shape of the

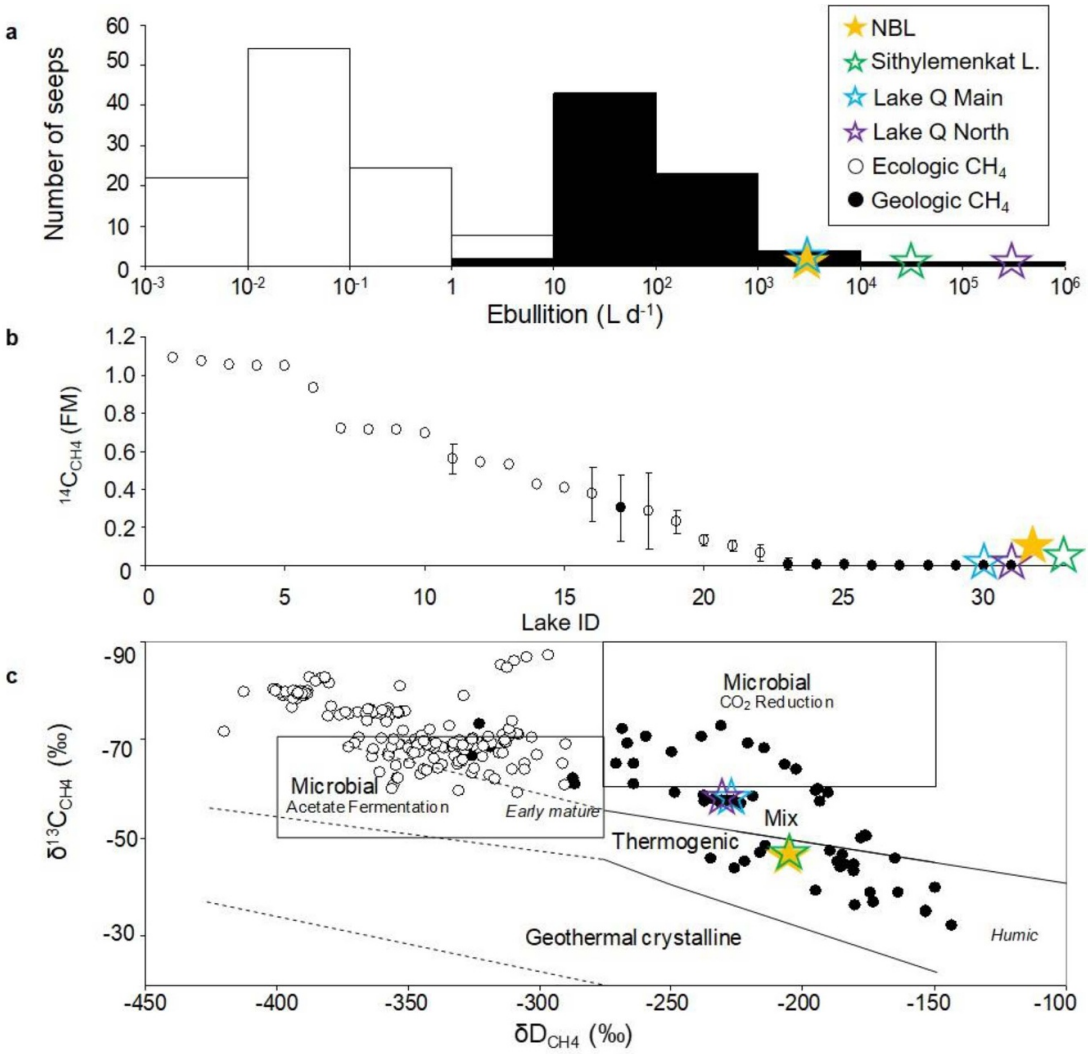

Figure 8. North Blair Lake (NBL) seep gas properties. Seepage magnitude (a), methane (CH_4) radiocarbon expressed as fraction modern (FM) carbon (b), and stable isotopes (c) of the NBL seep (yellow stars) plotted with other ecologic (open symbols) and geologic (black symbols) seeps in Alaska. Adapted from Walter Anthony *et al* (2012), with permission from Springer Nature.

ice/water interface from relatively slower ice growth beneath bubbles (Engram *et al* 2013, 2020).

The different sizes and density of seep-caused ice/water shapes will cause varying backscatter responses, since SAR backscatter depends on the height, horizontal size, and spacing of water-filled bumps in the ice, relative to the SAR wavelength (Ulaby and Long 2014). Several water-filled chimneys or bumps in the underside of the ice, less than a wavelength in size will seem 'rougher' than a single water-filled dome with a diameter much greater than a wavelength.

3.2.2. SAR detection of strong gas seepage in NBL

GPS points delineating the boundary of visible bubbling for the NBL seep in September 2021 correlated spatially to the perennial high L-band SAR σ^0 feature from lake ice (figure 6(b)). Seep area measured by the high SAR-backscatter area (5600–12 000 m^2, depending on early or late winter 2007–2011) was similar to mapped area from September 2021 fieldwork (8057 m^2). SAR was previously used in conjunction with local indigenous knowledge to discover new, large ^{14}C-depleted methane seeps (Walter Anthony *et al* 2012, Sullivan *et al* 2021). This is the first time SAR σ^0 was the only information used to guide us to a large methane seep for field work.

3.2.2.1. PALSAR-1 (L-band single-pol HH).

The NBL seep was visible as a group of distinct high (−5 to −10 dB maximum) σ^0 pixels in every single-pol PALSAR-1 image from 2006–2011 obtained during ice-cover. These 34 images were acquired with a variety of incidence angles throughout the winter (figure 9). Comparing σ^0 from pixels within the seep location (as defined by field GPS boundaries) for this dataset shows that the ranges of σ^0 from data acquired at 24° and 39° were the same; however, σ^0

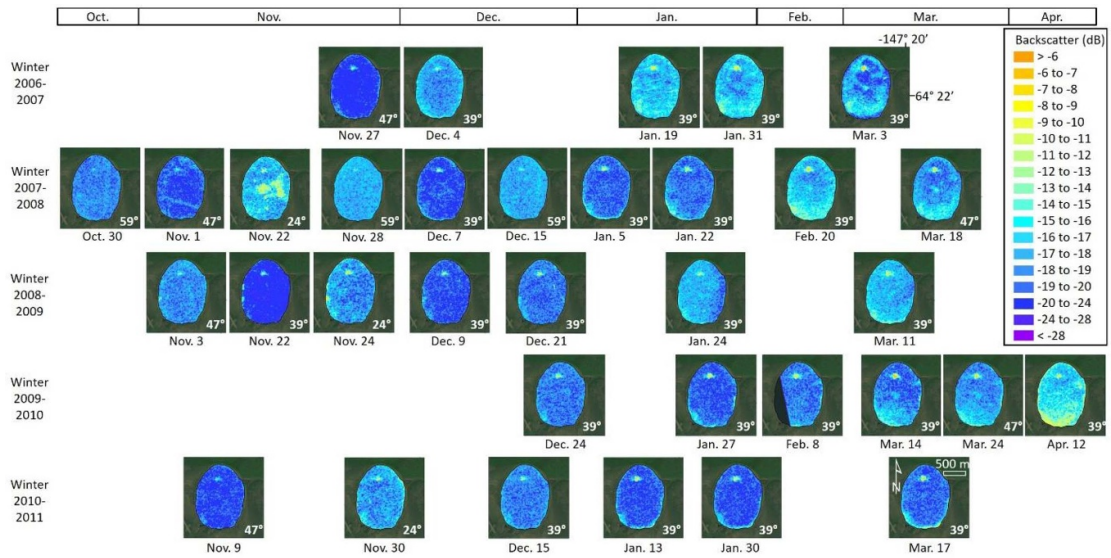

Figure 9. High backscatter anomaly (i.e. the bright feature in NW quadrant of NBL) is present in all available fine beam HH-polarized L-band scenes from 20 October to 15 April from PALSAR-1. Acquisition incidence angles noted in white text, lower right, of each scene. Data reproduced from © JAXA/METI ALOS PALSAR L1.5. Accessed through ASF DAAC 4 March 2022. Background images: ©2020 Maxar Technologies Inc., Alaska Geospatial Office, USGS.

decreased with increasing incidence angles (47° and 59°, table 2). Over the course of a winter, σ^0 from ice at the NBL seep acquired with 39° incidence angles increased (2007–2011, table 2). Backscatter trends over the winter from other incidence angles could not be compared due to lack of data.

In our effort to identify L-band imaging parameters most sensitive to gas seeps in lake ice, we found that scenes acquired with a 47° or a 24° incidence angle showed fairly high contrast in some scenes with less contrast in others; 59° was least sensitive (figure 9). Examining all PALSAR-1 Fine Beam Single-pol data acquired from 2006–2011 for visual contrast, images acquired with a 39° incidence angle consistently showed the seep clearly and were also regularly acquired by PALSAR-1 throughout the winter, creating a high temporal resolution dataset. This suggests that data acquired with a 39° incidence angle is the optimal imaging mode for L-band single polarized data from PALSAR-1.

3.2.2.2. JERS-1.

Older L-band data from the JERS-1 platform were all acquired with a 39° incidence angle from 1992–1996 and have a coarser spatial resolution (12.5 m pixel size compared to 6.25 m for single-pol PALSAR-1). The NBL seep field was visible in at least one scene per winter in all five winters' ice covers in JERS-1, although it was indistinguishable in three of the 15 scenes due to lack of contrast (high backscatter across the lake), and was only faintly visible in some early winter scenes (supplementary figure 3). The difference in seep visibility in these earlier data and PALSAR-1 data is most likely due to a higher noise floor in JERS-1 (noise equivalent sigma^0 is −14.5 dB, Shimada *et al* 2003) than PALSAR-1, resulting in less contrast and a noisier image overall in the older JERS-1 imagery. However, these data provide a valuable historical perspective, indicating that the NBL seep has existed since at least 1992. Similar to PALSAR-1 single-pol, JERS-1 backscatter from the NBL seep increased over the winter (1992–1997, table 3).

3.2.2.3. Sentinel-1 C-band

The NBL-seep ice returned high C-band σ^0 in both VV and VH polarizations throughout the winter of 2020–2021, showing visible contrast with surrounding ice in early winter for both polarizations (supplementary figure 4). Other researchers report larger (∼500 m diameter) low C-band σ^0 features appearing only in late winter from possible methane seeps in Western Siberia lakes, however no field confirmation that these were gas seeps was done (Pointner and Bartsch 2020, Pointner *et al* 2021). We see at NBL high σ^0 from both C- and L-band SAR starting in early winter from ground-truthed sub-permafrost methane seeps in frozen lakes with high σ^0 continuing all winter. The difference between these results can be explained by pressure from thick late-winter ice pushing water up through seeps in the West Siberian lake to cause large flooded areas on top of the ice, resulting in low backscatter. Further comparison of our results with previously published results are discussed in Supplementary Information: we show

Table 2. PALSAR-1 fine beam single-polarization (FBS) L-band backscatter intensity from the ice over the NBL seep from 34 scenes over 4 winters, varying incidence angles. Dashes indicate that no data were available over the site for that timeframe.

Season	FBS 24° (σ^0 dB)	n scenes/ n winters	FBS 39° (σ^0 dB)	n scenes/ n winters	FBS 47° (σ^0 dB)	n scenes/ n winters	FBS 59° (σ^0 dB)	n scenes/ n winters
Early winter (Oct–Dec)	−7 to −20	3/ 3	−7 to −20	7/ 6	−10 to −22	4/ 4	−12 to −21	3/ 1
Mid-winter (Jan–Feb)	—	—	−5 to −19	10/ 5	—	—	—	—
Spring (Mar–Apr)	—	—	−5 to −17	5/ 5	−5 to −15	2/ 2	—	—

Table 3. JERS-1 intensity from ice over the NBL seep from 15 scenes over 5 winters.

Season	JERS-1 39° (dB)	n scenes/n winters
Early winter (Oct–Dec)	−9 to −19	6/ 4
Mid-winter (Jan–Feb)	−7 to −18	5/ 4
Spring (Mar–Apr)	−7 to −17	4/ 3

midwinter high L-band σ^0 at feature locations on the West Siberia lake in supplementary figure 5.

3.2.3. SAR polarimetry from the NBL seep compared to other known geologic methane seeps in Alaskan lakes

The results of the two types of polarimetric decomposition (Pauli-based elements of [**T3**] coherency matrix vs. Yamaguchi 3-Component decomposition) were very similar, with visible differences in only four of 17 scenes (table 4, supplementary figure 6). In early winter, roughness and volumetric scattering were present at the site of the NBL seep for both decompositions (table 4).

All of the seeps, except for Q. Main, consistently demonstrated strong, distinct roughness scattering in every scene throughout the year. One reason for a less distinct, weaker roughness backscatter signal from the large Q. Main seep, is that this seep emerges as a single domed cavity (Walter *et al* 2009), creating one rough bump in the ice/water interface larger than one L-band SAR wavelength, a scenario which is governed by different scattering models than many bumps presenting in the same areal extent (Ulaby and Long 2014). Double-bounce was not detected on a regular basis in any of the seep shape types, indicating that the sides of water-filled ice columns are not orthogonal to the surrounding ice/water interface. Volumetric scattering was present only in the NBL seep on a regular basis. This is interesting since there is no appreciable volumetric component associated with ecologic seeps which often present as included bubbles in ice with a rough underlying ice/water interface (Engram *et al* 2012). One reason for a volumetric component at NBL lake could be the high density of bubbles in and under the ice. The presence of a volumetric component as well as roughness in the NBL seep could be leveraged to detect these types of seeps across a landscape.

3.2.4. Significance of high backscatter response and optimal SAR parameters

Since open water generally causes low-backscatter in SAR and open water is often present at these focused methane seeps, the high-backscatter response that we observed from field-confirmed sub-permafrost methane seeps in lake ice is surprising as well as useful. High backscatter indicates that the signal from the rough ice-water interface is stronger than low backscatter from any open water occurring at the surface of these seeps.

The determination of scattering mechanisms from quad-pol L-band SAR for large, sub-permafrost methane seeps in lake ice is significant information that could be used to evaluate the type of seep: roughness with a volumetric scattering component could mean a seep with mostly closed ice and bubbles included in the ice, similar to NBL seep, while a strong roughness signal could indicate a seep with multiple open holes, similar to Q-North and Sithylemenkat seeps. Other features in lake ice cause roughness scattering, such as ridges and cracks in the ice, but from our repeated observations of lake ice in SAR, they do not appear in the same location between years. Ecologic methane from decomposition of modern detritus also causes roughness scattering and could be responsible for backscatter variations across lake ice (Engram *et al* 2020); however, ecological ebullition is typically not focused in distinct anomalous features in lake ice, but rather appears as a more diffuse backscatter pattern.

L-band SAR showed consistent high backscatter from sub-permafrost methane seeps in lake ice. Seep pixels present as high contrast with surrounding ice throughout the winter. We observed slightly different scattering responses from differently shaped seep-ice (figure 2, table 4). C-band SAR shows high backscatter from seeps in early winter, but this signal is overshadowed by the high backscatter signal from floating lake ice in mid- and late-winter, especially in single-pol mode, limiting the usefulness of C-band to detect large methane seeps. The higher revisit frequency of Sentinel-1 does provide more opportunities for observing seeps in early winter: C-band is useful to confirm the presence of a known seep in the absence of L-band SAR.

Table 4. Comparison of polarimetric signals from seeps with different morphologies. Mean backscatter from seep is contrasted with backscatter with adjacent ice (100 m surrounding seep). Y3 indicates the Yamaguchi 3-component polarimetric decomposition. Backscatter units are σ^0 dB.

				Roughness		Double bounce		Volumetric Scattering	
Seep type	Seep name	Date PALSAR-1	Season	*T*11 Seep/Adj. Ice	Y3 Odd Seep/ Adj. Ice	*T*22 Seep/Adj. Ice	Y3 Dbl Seep/ Adj. Ice	*T*33 Seep/Adj. Ice	Y3 Vol Seep/Adj. Ice
Mostly closed ice with bubbles included, sometimes open holes in shoulder seasons	NBL	27-Nov-09	Fall	−10/−15[a]	−10/−15[a]	−20/−21	−20/−20	−22/−25[a]	−19/−20[a]
		12-Jan-08	Winter	−8/−15[a]	−8/−15[a]	−20/−22[a]	−19/−19	−23/−27[a]	−19/−19
		11-Apr-09	Spring	−6/−11[a]	−6/−11[a]	−16/−19[a]	−17/−18[a]	−19/−23[a]	−16/−18[a]
		14-Apr-10	Spring	−8/−11[a]	−9/−11[a]	−14/−16	−16/−17	−18/−21[a]	−16/−18[a]
Multiple open-holes	Lake Q North	13-Nov-09	Fall	−14/−21[a]	−15/−21[a]	−23/−24	−23/−23	−26/−28	−23/−23
		23-Mar-07	Spring	−10/−15[a]	−10/−15[a]	−21/−23[a]	−22/−22	−26/−27	−22/−22
		28-Mar-09	Spring	−10/−14[a]	−10/−14[a]	−22/−22	−22/−22	−24−24	−21/−21
		26-Apr-09	Spring	−7/−13[a]	−7/−13[a]	−20/−22	−22/−22	−22/−25[a]	−19/−21
Single open cavity, open hole	Lake Q Main	13-Nov-09	Fall	−13/−20[a]	−14/−20[a]	−24/−25	−23/−23	−27/−28	−23/−23
		23-Mar-07	Spring	−13/−12	−13/−12	−24/−22	−22/−22	−25/−24	−22/−21
		28-Mar-09	Spring	−13/−15	−14/−15	−22/−22	−22/−22	−25/−25	−21/−21
		26-Apr-09	Spring	−12/−16[a]	−13/−16	−23/−23	−22/−22	−26/−25	−22/−21
Two open holes, surrounded by included bubbles	Sithylemenkat	13-Nov-07	Fall	−15/−17[a]	−15/−17[a]	−23/−23	−20/−20	−27/−28	−20/−20
		29-Dec-07	Fall	−14/−19[a]	−13/−19[a]	−24/−25	−21/−21	−28/−29	−21/−21
		15-May-07	Spring	−5/−9[a]	−5/−9[a]	−18/−19	−19/−19	−21/−21	−18/−18
		30-Mar-08	Spring	−11/−14[a]	−11/−14[a]	−23/−24	−21/−21	−27/−29	−21/−21
		4-Apr-09	Spring	−10/−14[a]	−10/−14[a]	−22/−24	−20/−20	−27/−29	−20/−20

[a] indicates seep is visibly distinct from surrounding lake ice.

4. Conclusion

Large uncertainties regarding past and present ^{14}C-depeleted methane contribution from natural sources still exist (Etiope and Schwietzke 2019, Dyonisius *et al* 2020, Hmiel *et al* 2020), making accurate prediction of the quantity of sub-permafrost methane release with future permafrost disintigration impossible. A new remote sensing tool to detect and monitor methane seeps in lakes would be a valuable asset to climate science.

The discovery of a large methane seep at NBL demonstrates that SAR remote sensing can detect large gas seeps in frozen lakes across a landscape. Although seeps were discernable in C-band SAR, L-band SAR showed more contrast between the seep and surrounding ice throughout the winter. High backscatter must appear perennially in L-band SAR to be considered a potential seep indicator: data acquired with a 39° incidence angle gave the best results. Other non-seep features such as cracks and ridges in lake ice return ephemeral high backscatter, but will not perennially appear in the same location: these features appear in different locations between years. Confirmation of a possible seep with optical/multispectral imagery is recommended, although seeps will not necessarily appear as holes in the ice when obscured by a thin layer of ice and snow. Remote sensing SAR and optical imagery cannot determine the chemical composition of a gas seep, but they can guide field work where samples can be collected for analyses.

Methane origin of the NBL seep was inconclusive. Ebullition magnitude, stable isotope values and the radiocarbon age of methane were consistent with a geologic (potentially thermogenic) source; however, the low methane concentration in the bubbles was atypical of other thermogenic seeps previously sampled in Alaskan lakes (Walter Anthony *et al* 2012) and more similar to the bubble geochemistry in another uniquely round shaped lake in the Brooks Range, Sithylemenkat Lake. Historic JERS-1 SAR data show that the seep has existed at least since 1992.

We show that seeps with different ice-bubble morphologies return different types of SAR polarimetric parameters as determined by two different polarimetric decompositions. This information could be useful for categorizing newly-discovered seeps based on the link between SAR scattering mechanisms and the physical and spatial presentation of known geologic methane seeps. Mapping and monitoring such seeps with remote sensing could also be used to provide thin-ice hazard maps for people traveling across frozen landscapes in winter and improving our understanding of natural geologic methane emissions to the atmosphere.

The new NASA-Indian Space Research Organization Synthetic Aperture Radar mission, planned to launch in 2024, will provide dual-pol L-band SAR data with more frequent revisit times than PALSAR and open data access that can detect large gas seeps in lakes to (1) target for field sampling and potential travel hazard, and (2) monitor for increase in size and number of naturally occurring seeps. Field sampling and analysis at sites located by SAR and confirmed with optical imagery will further our knowledge of the contribution of ^{14}C-depleted methane to the atmosphere now and in the future.

Data availability statement

All data that support the findings of this study are included within the article (and any supplementary files), or are publically available.

Acknowledgments

The authors gratefully acknowledge the Alaska Satellite Facility (ASF) for providing SAR data and post-processing tools (MapReady), the Alaska Division of Geological and Geophysical Surveys for providing elevation data for SAR terrain correction, and the European Space Agency for providing Sentinel-1 data and post-processing tools (SNAP) as well as SAR polarimetric processing tools (PolSARPro). For invaluable field measurements at North Blair Lake, we thank P Hanke, A Bondurant, P Anthony, A Anthony, J Anthony. We thank M T Aguirrezabala Cámpano for assistance in LGR gas chamber data processing. R Bursiel at Wright Air Service described observing the seeps, which he assumed were springs, during overflights. The authors thank Barrett Salisbury, geologist at the Alaska State Division of Geological and Geophysical Surveys for his expert insight on the Blair Lakes fault.

Funding source

This work was perfomed for the *'Characterizing Microtopographic Hot-spots and Landscape-scale Methane Emissions Across the ABoVE Domain'*, a Phase 2 project of NASA's Arctic-Boreal Vulnerability Experiment (ABoVE) awarded to the Jet Propulsion Laboratory, California Institute of Technology (80NM0018D0004) and the University of Alaska Fairbanks.

ORCID iDs

Melanie Engram https://orcid.org/0000-0002-1144-1827
Katey Walter Anthony https://orcid.org/0000-0003-2079-2896

References

Aguirrezabala-Campano T, Gonzalez-Valencia R, Cervantes F J and Thalasso F 2021 Overall spatiotemporal dynamics of

greenhouse gasses and oxygen in two subtropical reservoirs with contrasting trophic states *Water Res.* **196** 117056
Atwood D K, Gunn G E, Roussi C, Wu J, Duguay C and Sarabandi K 2015 Microwave backscatter from Arctic lake ice and polarimetric implications *IEEE Trans. Geosci. Remote* **53** 5972–82
Beget J E, Hopkins D M and Charron S D 1996 The largest known Maars on earth, Seward Peninsula, northwest Alaska *Arctic* **49** 62–69
Bowen R G, Dallimore S R, Côté M M, Wright J F, Lorenson T D, Kane D L and Hinkel K M 2008 Geomorphology and gas release from pockmark features in the Mackenzie Delta, Northwest Territories, Canada *Proc. 9th Int. Conf. on Permafrost* (University of Alaska)
Cannon P J 1977 Meteorite impact crater discovered in Central Alaska with landsat imagery *Science* **196** 1322–4
Cannon P J 1978 Response: meteorite impact crater in central Alaska *Science* **201** 279–80
Chacho E F, Arcone S A, Delaney A J, Arcone S A and Delaney A J 1995 *Blair Lakes Target Facility Permafrost and Groundwater Study* (U.S. Army Cold Regions Research and Engineering Laboratory)
Dyonisius M N *et al* 2020 Old carbon reservoirs were not important in the deglacial methane budget *Science* **367** 907–10
Elder C D, Thompson D R, Thorpe A K, Chandanpurkar H, Hanke P J, Hasson N, James S R, Minsley B J, Pastick N J and Olefeldt D 2021 Characterizing methane emission hotspots from thawing permafrost *Glob. Biogeochem. Cycles* **35** e2020GB006922
Elder C D, Thompson D R, Thorpe A K, Hanke P, Walter Anthony K M and Miller C E 2020 Airborne mapping reveals emergent power law of arctic methane emissions *Geophys. Res. Lett.* **47** e2019GL085707
Engram M, Anthony K W, Meyer F J and Grosse G 2012 Synthetic aperture radar (SAR) backscatter response from methane ebullition bubbles trapped by thermokarst lake ice *Can. J. Remote Sens.* **38** 667–82
Engram M, Anthony K W, Meyer F J and Grosse G 2013 Characterization of L-band synthetic aperture radar (SAR) backscatter from floating and grounded thermokarst lake ice in Arctic Alaska *Cryosphere* **7** 1741–52
Engram M, Walter Anthony K M, Sachs T, Kohnert K, Serafimovich A, Grosse G and Meyer F J 2020 Remote sensing northern lake methane ebullition *Nat. Clim. Change* **10** 511–7
Etiope G and Klusman R W 2002 Geologic emissions of methane to the atmosphere *Chemosphere* **49** 777–89
Etiope G and Martinelli G 2002 Migration of carrier and trace gases in the geosphere: an overview *Phys. Earth Planet. Inter.* **129** 185–204
Etiope G and Schwietzke S 2019 Global geological methane emissions: an update of top-down and bottom-up estimates *Elementa* **7** 47
Ferguson J E and Gunn G E 2022 Polarimetric decomposition of microwave-band freshwater ice SAR data: review, analysis, and future directions *Remote Sens. Environ.* **280** 113176
Frankenberg C *et al* 2016 Airborne methane remote measurements reveal heavy-tail flux distribution in Four Corners region *Proc. Natl Acad. Sci. USA* **113** 9734–9
Gedney L D and VanWormer J D 1974 Evaluation of feasibility of mapping seismically active faults in Alaska *NASA-CR-138679 Technical Report: National Aeronautics and Space Administration, Goddard Space Flight Center* (Geophysical Institute, University of Alaska Fairbanks)
Gieck R E and Kane D L 1986 Hydrology of two subarctic satershets paper presented at cold regions hydrology *Cold Regions Hyydrology. American Water Resources Association* ed D L Kane (University of Alaska Fairbanks) pp 283–91
Hmiel B *et al* 2020 Preindustrial $^{14}CH_4$ indicates greater anthropogenic fossil CH_4 emissions *Nature* **578** 409–12
Isaksen I S A, Gauss M, Myhre G, Walter Anthony K M and Ruppel C 2011 Strong atmospheric chemistry feedback to climate warming from Arctic methane emissions *Glob. Biogeochem. Cycles* **25** GB2002
Jorgenson M T, Racine C H, Walters J C and Osterkamp T E 2001 Permafrost degradation and ecological changes associated with a warming climate in in central Alaska *Clim. Change* **48** 551–79
Jorgenson T, Yoshikawa K, Kanevskiy M, Shur Y, Romanovsky V, Marchenko S, Grosse G, Brown J and Jones B 2008 Permafrost characteristics of Alaska *Proc. Ninth Int. Conf. on Permafrost* ed D L Kane and K M Hinkel map in scale 1:7,000,000 (Institute of Northern Engineering, Fairbanks AK)
Kane D L 1981 Groundwater recharge in cold regions *Northern Eng.* **13** 28–33
Kleber G E, Hodson A J, Magerl L, Mannerfelt E S, Bradbury H J, Zhu Y, Trimmer M and Turchyn A V 2023 Groundwater springs formed during glacial retreat are a large source of methane in the high Arctic *Nat. Geosci.* **16** 597–604
Kohnert K, Serafimovich A, Metzger S, Hartmann J and Sachs T 2017 Strong geologic methane emissions from discontinuous terrestrial permafrost in the Mackenzie Delta, Canada *Sci. Rep.* **7** 1–6
Komarov V, Wang S and Tang J 2005 Permittivity and measurements *Encyclopedia of RF and Microwave Engineering* ed K Chang (Wiley) pp 3693–711
Kurtz M K, Benfer R H, Christopher W G, Franenstein G E, Ban Wyhe G and Roguski E A 1966 Consolidated report, operation breakup, FY66: NCG/TM 66–7: ice cratering experiments, Blair Lake, Alaska (U.S. Army)
Lorenz V 1973 On the Formation of Maars *Bull. Volcanol.* **37** 183–204
Masterson W D, Dzou L I P, Holba A G, Fincannon A L and Ellis L 2001 Evidence for biodegradation and evaporative fractionation in West Sak, Kuparuk and Prudhoe Bay field areas, North Slope, Alaska *Org. Geochem.* **32** 411–41
Mätzler C and Wegmüller U 1987 Dielectric properties of fresh-water ice at microwave frequencies *J. Phys. D: Appl. Phys.* **21** 1623–30
Mazzini A, Sciarra A, Etiope G, Sadavarte P, Houweling S, Pandey S and Husein A 2021 Relevant methane emission to the atmosphere from a geological gas manifestation *Sci. Rep.* **11** 4138
Messager M L, Lehner B, Grill G, Nedeva I and Schmitt O 2016 Estimating the volume and age of water stored in global lakes using a geo-statistical approach *Nat. Commun.* **7** 13603
Miller C E *et al* 2019 An overview of ABoVE airborne campaign data acquisitions and science opportunities *Environ. Res. Lett.* **14** 080201
Murfitt J and Duguay C R 2021 50 years of lake ice research from active microwave remote sensing: progress and prospects *Remote Sens. Environ.* **264** 112616
Myhre G *et al* 2013 Climate change 2013: the physical science basis *Contribution of Working Group I to the Fifth Assessment Report of the Intergovernmental Panel on Climate Change* ed T F Stocker, D Qin, G-K Plattner, M Tignor, S K Allen, J Boschung, A Nauels, Y Xia, V Bex and P M Midgley (Cambridge University Press)
Patton W W and Miller T P 1978 Response: meteorite impact crater in central Alaska *Science* **201** 279–80
Paull Charles K, Dallimore Scott R, Jin Young K, Caress David W, Lundsten E, Gwiazda R, Anderson K, Hughes Clarke J, Youngblut S and Melling H 2022 Rapid seafloor changes associated with the degradation of Arctic submarine permafrost *Proc. Natl Acad. Sci. USA* **119** e2119105119
Planet Team 2017 Planet application program interface *Space for Life on Earth* (available at: https://api.planet.com)
Pointner G and Bartsch A 2020 Interannual variability of lake ice backscatter anomalies on lake Neyto, Yamal, Russia *GI_Forum* **8** 47–62

Pointner G, Bartsch A, Dvornikov Y A and Kouraev A V 2021 Mapping potential signs of gas emissions in ice of Lake Neyto, Yamal, Russia, using synthetic aperture radar and multispectral remote sensing data *Cryosphere* **15** 1907–29

Schwietzke S *et al* 2016 Upward revision of global fossil fuel methane emissions based on isotope database *Nature* **538** 88–91

Shimada T, Kawamura H and Shimada M 2003 An L-band geophysical model function for SAR wind retrieval using JERS-1 SAR *IEEE Trans. Geosci. Remote* **41** 518–31

Strauss J *et al* 2022 Database of ice-rich yedoma permafrost version 2 (IRYP v2) *Pangaea*

Sullivan T D, Parsekian A D, Sharp J, Hanke P J, Thalasso F, Shapley M, Engram M and Walter Anthony K 2021 Influence of permafrost thaw on an extreme geologic methane seep *Permafr. Periglac.* **32** 484–502

Ulaby F and Long D 2014 *Microwave Radar and Radiometric Remote Sensing* (University of Michigan Press)

von Fischer J C, Rhew R C, Ames G M, Fosdick B K and von Fischer P E 2010 Vegetation height and other controls of spatial variability in methane emissions from the Arctic coastal tundra at Barrow, Alaska *J. Geophys. Res.* **115** G4

Walter Anthony K M *et al* 2021 Decadal-scale hotspot methane ebullition within lakes following abrupt permafrost thaw *Environ. Res. Lett.* **16** 035010

Walter Anthony K M, Anthony P, Grosse G and Chanton J 2012 Geologic methane seeps along boundaries of Arctic permafrost thaw and melting glaciers *Nat. Geosci.* **5** 419–26

Walter K, Witmer D and Holdmann G 2009 *Final Report: Field Exploration of Methane Seep Near Atqasuk* (University of Alaska Fairbanks for Dept. of Energy)

Woo M-K 2012 *Permafrost Hydrology* (Springer)

Wooller M J, Pohlman J W, Gaglioti B V, Langdon P, Jones M, Walter Anthony K M, Becker K W, Hinrichs K-U and Elvert M 2012 Reconstruction of past methane availability in an Arctic Alaska wetland indicates climate influenced methane release during the past ∼12,000 years *J. Paleolimnol.* **48** 27–42

Yakushev V S and Chuvilin E M 2000 Natural gas and gas hydrate accumulations within permafrost in Russia *Cold Reg. Sci. Technol.* **31** 189–97

Yamaguchi Y, Yajima Y and Yamada H 2006 A four-component decomposition of POLSAR images based on the coherency matrix *IEEE Geosci. Remote* **3** 292–6

Yoshikawa K and Hinzman L D 2003 Shrinking thermokarst ponds and groundwater dynamics in discontinuous permafrost near Council, Alaska *Permafr. Periglac.* **14** 151–60

Youcha E K 2003 A geohydrologic analysis of an upland-bedrock aquifer system: applications to interior Alaska *Thesis* (College of Science, Engineering, and Mathematics. University of Alaska, Fairbanks)

Zimov S A, Voropaev Y V, Davydov S P, Zimova G M, Davydova A I, Chapin I I I F S and Chapin M C 2001 Flux of methane from north Siberian aquatic systems: influence on atmospheric methane *Permafrost Response on Economic Development, Environmental Security and Natural Resources* (Kluwer Academic Publishers, Dordrecht, Netherlands)